

Symmetry-enforced double Weyl points, multiband quantum geometry, and singular flat bands of doping-induced states at the Fermi level

Moritz M. Hirschmann^{1,*} and Johannes Mitscherling^{2,*}

¹*RIKEN Center for Emergent Matter Science, Wako, Saitama 351-0198, Japan*

²*Department of Physics, University of California, Berkeley, California 94720, USA*

(Dated: January 31, 2025)

Two common difficulties in the design of topological quantum materials are that the desired features lie too far from the Fermi level and are spread over a too-large energy range. Doping-induced states at the Fermi level provide a solution, where nontrivial topological properties are enforced by the doping-reduced symmetry. To show this, we consider a regular placement of dopants in a lattice of space group (SG) 176 ($P6_3/m$), which reduces the symmetry to SG 143 ($P3$). Our two- and four-band models feature double Weyl points, Chern bands, Van Hove singularities, nontrivial multiband quantum geometry due to mixed orbital character, and singular flat bands. We relate these features to density-functional theory (DFT) calculations for dopant and vacancy bands of lead apatite $\text{Pb}_{10}(\text{PO}_4)_6\text{O}$ and $\text{Pb}_{10}(\text{PO}_4)_6(\text{OH})_2$, the van der Waals ferromagnet $\text{Cr}_2\text{Ge}_2\text{Te}_6$, the semiconductor SiC , and the 2D dichalcogenide MoS_2 .

I. INTRODUCTION

Two difficulties in the study of topological band theory [1, 2] are that (i) the topological features [3–5] lie too far from the Fermi level and (ii) are spread over a too-large energy range. Challenge (i) can be addressed by extensive material surveys [6–8], by pushing interstitial electrons into the gap of a molecular crystal [9], or by defect states, within a gap in the vicinity of the Fermi level [10–13]. Difficulty (ii) can be avoided by narrow bands, which are known to occur in hexagonal systems [4, 14, 15]. Systems with narrow and flat bands have attracted broad interest in the last years [16–29] due to their interplay of quantum geometry and strong correlations. Besides the well-known Berry curvature, in particular the quantum metric—a distance measure between Bloch states of close-by momenta [30]—relates to a diverse set of phenomena [31–47], which is particularly important in the context of narrow or flat bands [42–45].

To tackle the two aforementioned difficulties in finding geometric narrow bands near the Fermi level, we build on the idea of combining doping-induced in-gap states with symmetry-enforced topology. Our approach is inspired by density-functional theory (DFT) calculations on pristine copper-doped lead apatite $\text{Pb}_9\text{Cu}(\text{PO}_4)_6(\text{OH})_2$ [48] and $\text{Pb}_9\text{Cu}(\text{PO}_4)_6\text{O}$ [49–51] that assumed the regular replacement of one of the four lead atoms on the $4f$ Wyckoff positions by copper. We show that the DFT band structure [48, 49] provides precisely an example of the desired scenario with a topological band structure that arises due to the SG 143 ($P3$) of the assumed copper-doped crystal structure. Whereas this arrangement of dopants has not yet been realized experimentally in copper-doped lead apatite [52], we identify doped $\text{Cr}_2\text{Ge}_2\text{Te}_6$ [53–55], doped SiC [56–58], and sulfur vacan-

cies in MoS_2 [59–61] as candidates of analogous doping-induced topological bands.

To describe the above systems, we construct minimal two- and four-band tight-binding models, for which we identify key topological and quantum geometric features, including double Weyl points, Chern bands, nontrivial Berry curvature, and a nonzero quantum metric for single and combined sets of connected bands due to orbital mixing, and singular flat bands. The flatness occurs due to destructive interference [26, 62–70], which resembles a higher-dimensional version of the Creutz ladder [71] and enables further studies of its unique physics [15, 31, 45, 72–87] in combination with the nontrivial multiband quantum geometry.

II. MINIMAL TIGHT-BINDING MODELS

We consider the rich topology of SG 176 ($P6_3/m$), the SG of lead apatite [88, 89]. It enforces band crossings on points, lines, and planes [90, 91]. For spinful bands this centrosymmetric group leads to three Dirac nodal lines intersecting at the A point as a result of the off-centered mirror symmetry m_z [92]. Systems with spinless representations of $P6_3/m$ exhibit always a nodal plane at $k_z = \pi$ [93] and Dirac points at $k_z = 0$ are possible [90].

With doping one site per unit cell one should expect that the space group symmetry is in general reduced. In the absence of a significant structural transition, the new band structure exhibits still the (symmorphic) site symmetry. Specifically, substituting one copper on the $4f$ Wyckoff position of lead-apatite, as assumed in DFT [48–51], reduces SG 176 to SG 143 ($P3$) with broken inversion symmetry [94]. The complex spinless representation of $P3$ provides the minimal model for just a pair of Weyl points at the time-reversal invariant momenta (TRIMs) Γ and A. In contrast, the spinful representations are known to exhibit eight Kramers-Weyl points [95].

* These authors contributed equally to this work.

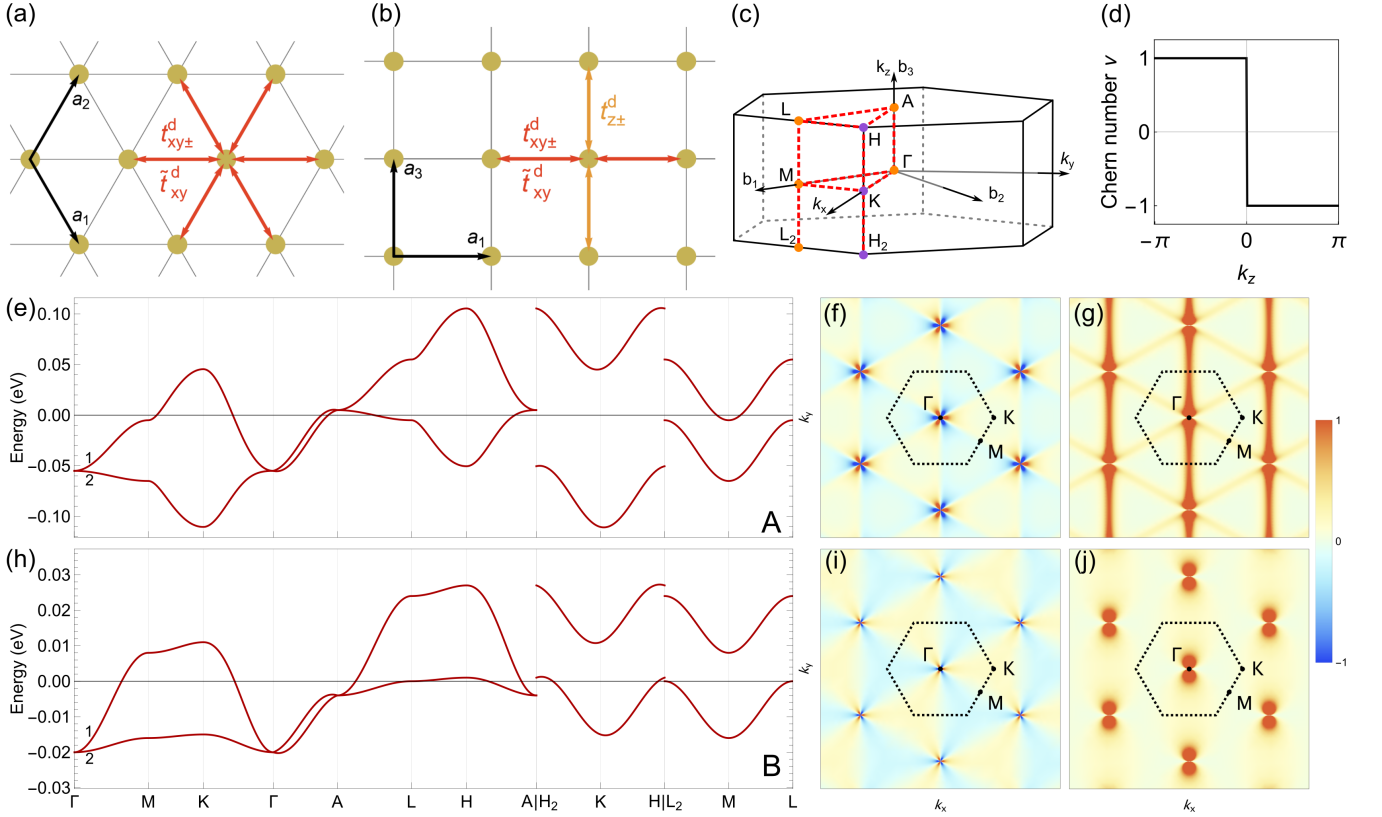


FIG. 1. **Two-band model for SG $P3$.** [(a),(b)] Top and side view of the trigonal lattice with nearest-neighbor hopping terms, where symmetry-related directions are shown in the same color. (c) Brillouin zone with TRIMs (orange), high-symmetry points (purple), and k -path (red) that is used for the band structures with parameter sets A and B in (e) and (h), respectively. The parameters are summarized in Table I. (d) Symmetry-enforced Chern numbers on planes of constant k_z . Berry curvature Ω_2^{xy} [(f),(i)] and quantum metric g_2^{xx} [(g),(j)] at $k_z = 0$ corresponding to the models to the left.

A. Two-band model

To construct an effective model for the doping-induced states in a lattice of SG $P6_3/m$, we assume that the relevant states form a lattice with SG $P3$. Without loss of generality, they occupy the 1a Wyckoff position of the trigonal unit cell. We introduce all symmetry-allowed nearest-neighbor hopping terms, see Figs. 1(a) and 1(b). To capture the band topology in a symmetry-enforced fashion, we use the complex representation of the three-fold rotation C_3 , created by the operators $\{\hat{d}_1^\dagger, \hat{d}_2^\dagger\}$ corresponding to the rotation eigenvalues $e^{2\pi i/3}$ and $e^{-2\pi i/3}$, respectively. This can capture any band pair comprising d_{xz^-} , d_{yz^-} , $d_{x^2-y^2^-}$, and d_{xy} -orbital weights, see Appendix A 1. We find the Hamiltonian

$$H_d(\mathbf{k}) = \begin{pmatrix} H_{11}(\mathbf{k}) & H_{12}(\mathbf{k}) \\ H_{12}^*(\mathbf{k}) & H_{22}(\mathbf{k}) \end{pmatrix} \quad (1)$$

with

$$H_{11}(\mathbf{k}) = -\mu_d + t_{z+}^d \cos(\mathbf{k} \cdot \mathbf{a}_3) + t_{z-}^d \sin(\mathbf{k} \cdot \mathbf{a}_3) \\ + t_{xy+}^d \left[\cos(\mathbf{k} \cdot \mathbf{a}_1) + \cos(\mathbf{k} \cdot (\mathbf{a}_1 + \mathbf{a}_2)) + \cos(\mathbf{k} \cdot \mathbf{a}_2) \right]$$

$$+ t_{xy-}^d \left[\sin(\mathbf{k} \cdot \mathbf{a}_1) - \sin(\mathbf{k} \cdot (\mathbf{a}_1 + \mathbf{a}_2)) + \sin(\mathbf{k} \cdot \mathbf{a}_2) \right], \quad (2)$$

$$H_{22}(\mathbf{k}) = H_{11}(-\mathbf{k}), \quad (3)$$

$$H_{12}(\mathbf{k}) = \tilde{t}_{xy}^d \left[\cos(\mathbf{k} \cdot \mathbf{a}_1) + e^{i\frac{2\pi}{3}} \cos(\mathbf{k} \cdot (\mathbf{a}_1 + \mathbf{a}_2)) \right. \\ \left. + e^{-i\frac{2\pi}{3}} \cos(\mathbf{k} \cdot \mathbf{a}_2) \right], \quad (4)$$

where we use the lattice vectors $\mathbf{a}_1 = a(1/2, -\sqrt{3}/2, 0)$, $\mathbf{a}_2 = a(1/2, \sqrt{3}/2, 0)$, and $\mathbf{a}_3 = c(0, 0, 1)$, setting $a = c = 1$. The model has six parameters, the \mathbf{a}_1 - \mathbf{a}_2 -plane hoppings $t_{xy\pm}^d$ and \tilde{t}_{xy}^d , the out-of-plane hoppings $t_{z\pm}^d$, and the chemical potential μ_d . The subscripts denote the real space directions and whether the hopping is inversion symmetric (+) or antisymmetric (-). We provide longer-range hoppings and the Hamiltonian in real space in the Appendixes A 2 and A 3. Two band structures along the path sketched in Fig. 1(c) are shown in Figs. 1(e) and 1(h) for different parameter sets, see Table I.

The band gap vanishes at Γ and A independent of parameters, as enforced by time-reversal symmetry. The gaps at M and L (K and H) are identical and scale with $|t_{xy}^d|$ ($|t_{xy-}^d|$). The splitting on Γ -A is proportional to $|t_{z-}^d|$. The comparison of the band curvatures at the band

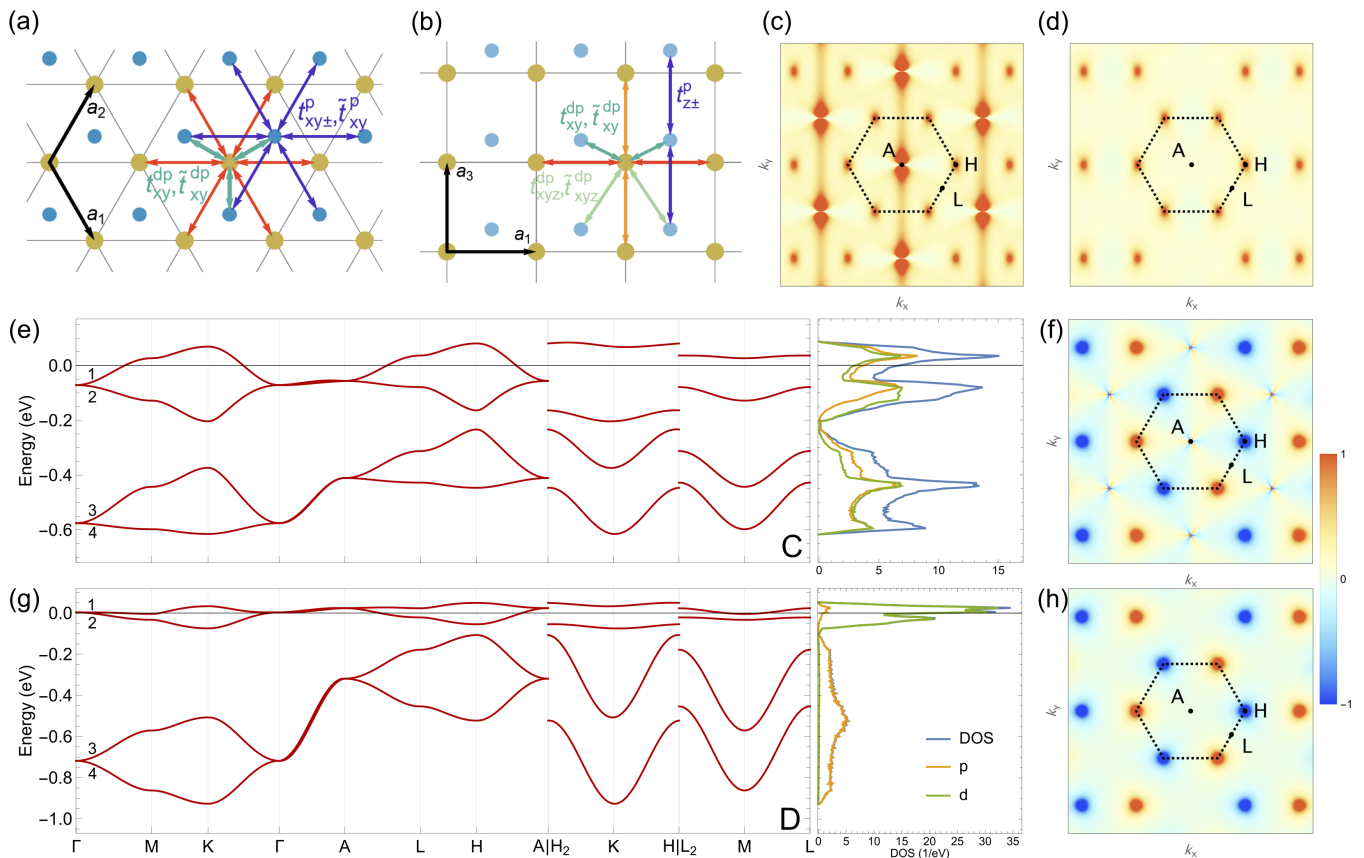


FIG. 2. **Four-band model for SG $P3$.** [(a),(b)] Top and side view of the trigonal lattice with nearest- and next-nearest-neighbor hopping terms, where symmetry-related directions are shown in the same color. (e,g) Resulting band structures with the corresponding (orbital-resolved) density of states (DOS) for parameter sets C and D, see Table I. [(c),(d)] Quantum metric g^{xx} for band 2 and bands (12) with parameter set C. [(f),(h)] Berry curvature Ω^{xy} for bands 2 and (12) with parameter set C.

touching points Γ and A give insight into the sign of t_{xy}^d and its relative size compared to $|\tilde{t}_{xy}^d|$, see Appendix A 4.

B. Four-band model

Inspired by the hybridization between the copper Cu and extra oxygen O or $(\text{OH})_2$ orbitals, as seen in DFT [48–51], we introduce a second site to our lattice on the 1b Wyckoff position of space group $P3$. The resulting second band pair exhibits the complex representation of $P3$, referred to as $\{\hat{p}_1^\dagger, \hat{p}_2^\dagger\}$. This can capture any band pair comprising p_x - and p_y -orbital weights. Our four-band model takes the form

$$H_{4 \times 4}(\mathbf{k}) = \begin{pmatrix} H_d(\mathbf{k}) & H_{dp}(\mathbf{k}) \\ H_{dp}^\dagger(\mathbf{k}) & H_p(\mathbf{k}) \end{pmatrix}. \quad (5)$$

The hopping terms, see Figs. 2(a) and 2(b), within each sublattice take the same form as in the two-band model. Thus, we keep $H_d(\mathbf{k})$ for the d sublattice and define $H_p(\mathbf{k})$ for the p sublattice by replacing $d \rightarrow p$ in all indices of $H_d(\mathbf{k})$ in Eq. (1). We give the exact form of the inter-sublattice hopping $H_{dp}(\mathbf{k})$ in Appendix B 1, the

symmetries and basis convention in Appendix B 2, and the real space description in Appendix B 3. Two band structures are shown in Figs. 2(e) and 2(g) for different parameter sets, see Table I.

III. RESULTS

A. Topology and quantum geometry

In a multiband system, not only the band dispersion but also the quantum states generically exhibit a nontrivial momentum dependence, which is described by quantum geometry locally and topology globally. We introduce the projector formalism for multiband quantum geometry and apply it to the two- and four-band models.

1. Projector formalism for multiband quantum geometry

We use the convenient mathematical description in terms of band projectors $P_n(\mathbf{k}) = |u_n(\mathbf{k})\rangle\langle u_n(\mathbf{k})|$ [39–41] with the defining property $P_n(\mathbf{k})P_m(\mathbf{k}) = \delta_{nm}P_n(\mathbf{k})$.

The projectors are unaffected by the $U(1)$ gauge ambiguity of the cell-periodic Bloch wave function $|u_n(\mathbf{k})\rangle$ of each band n . Single-band projectors are not well defined at the momenta of band touching. Thus, in addition to the projectors of each band, we construct the projector on two bands isolated from the rest, i.e., $P_{(12)}(\mathbf{k}) = P_1(\mathbf{k}) + P_2(\mathbf{k})$. This projector on the subsystem is gauge invariant under $U(2)$ gauge transformations [40]. Even if there are band crossings between the two bands, the projector $P_{(12)}$ will be well defined for all momenta.

A projector $P_j(\mathbf{k})$ on a single band or larger subspace defines the corresponding quantum metric $g_j^{\alpha\beta}(\mathbf{k})$ and Berry curvature $\Omega_j^{\alpha\beta}(\mathbf{k})$ via

$$g_j^{\alpha\beta}(\mathbf{k}) = \frac{1}{2} \text{Tr} \left[\partial_\alpha P_j(\mathbf{k}) \partial_\beta P_j(\mathbf{k}) \right], \quad (6)$$

$$\Omega_j^{\alpha\beta}(\mathbf{k}) = i \text{Tr} \left[P_j(\mathbf{k}) \partial_\alpha P_j(\mathbf{k}) \partial_\beta P_j(\mathbf{k}) \right] - (\alpha \leftrightarrow \beta), \quad (7)$$

with trace Tr and momentum derivative $\partial_\alpha = \partial_{k_\alpha}$ in direction α . Note that the quantum metric is in general nonadditive, that is $g_{(12)}^{\alpha\beta} = g_1^{\alpha\beta} + g_2^{\alpha\beta} + \text{Tr}[\partial_\alpha P_1 \partial_\beta P_2]$ when $P_{(12)} = P_1 + P_2$, where the last cross term involves the projector of both bands 1 and 2 [40].

A two-band Hamiltonian in the Bloch basis can be written in the form $H(\mathbf{k}) = d_0(\mathbf{k}) + d_x(\mathbf{k})\sigma_x + d_y(\mathbf{k})\sigma_y + d_z(\mathbf{k})\sigma_z$ with Pauli matrices σ_x, σ_y , and σ_z and momentum-dependent functions $d_0(\mathbf{k}), d_x(\mathbf{k}), d_y(\mathbf{k})$, and $d_z(\mathbf{k})$. We do not write the identity matrix explicitly. It is useful to define $d(\mathbf{k}) = \sqrt{d_x(\mathbf{k})^2 + d_y(\mathbf{k})^2 + d_z(\mathbf{k})^2}$. The projectors onto the two bands take the form $P_\pm(\mathbf{k}) = \frac{1}{2}(1 \pm \mathbf{n}(\mathbf{k}) \cdot \boldsymbol{\sigma})$, where $\mathbf{n}(\mathbf{k}) = (d_x(\mathbf{k}), d_y(\mathbf{k}), d_z(\mathbf{k}))/d(\mathbf{k})$ and $\boldsymbol{\sigma} = (\sigma_x, \sigma_y, \sigma_z)$ leading to the commonly used expressions $g_\pm^{\alpha\beta}(\mathbf{k}) = \frac{1}{4} \partial_\alpha \mathbf{n}(\mathbf{k}) \cdot \partial_\beta \mathbf{n}(\mathbf{k})$ and $\Omega_\pm^{\alpha\beta}(\mathbf{k}) = \mp \frac{1}{2} \mathbf{n}(\mathbf{k}) \cdot (\partial_\alpha \mathbf{n}(\mathbf{k}) \times \partial_\beta \mathbf{n}(\mathbf{k}))$. Note that the quantum metrics of both bands are identical and the Berry curvatures have opposite signs.

The numerical evaluation of the quantum metric and Berry curvature in the projector formalism is straightforward. For a fixed momentum, we obtain the complex vector $|u_n(\mathbf{k})\rangle$ by diagonalizing $H(\mathbf{k})$ numerically and construct the respective projector matrix. The gauge invariance enables the use of discrete derivatives of the projectors, i.e., $\partial_x P_j(\mathbf{k}) \approx \frac{1}{2\delta} [P_j(k_x + \delta, k_y, k_z) - P_j(k_x - \delta, k_y, k_z)]$ for sufficiently small $\delta > 0$. Numerical accuracy can be checked by projector identities such as $(\partial_x P_n(\mathbf{k}))P_m(\mathbf{k}) + P_n(\mathbf{k})(\partial_x P_m(\mathbf{k})) = 0$ for $n \neq m$.

2. Application to the two- and four-band models

As expected for spinless representations [96, 97], we find double Weyl points with Chern number $\nu = -2$ and $\nu = +2$ at Γ and A, respectively, as shown in Fig. 1(d) [98]. We show the Berry curvature Ω_2^{xy} in Figs. 1(f) and 1(i) and the quantum metric g_2^{xx} in Figs. 1(g) and 1(j) for $k_z = 0$ and band 2, where the Weyl points lead to

divergences. Depending on the gap size on Γ -A, see Appendix A 4, the Berry curvature in Fig. 1(f) is larger compared to Fig. 1(i). Whereas the quantum metric is only large around Γ in Fig. 1(j), it has extended regions with larger contributions in Fig. 1(g). To illustrate that the dependence on the Γ -A gap is a generic feature, we discuss the plane $k_z = \pi/2$ in Appendix A 5. More than two bands are required to see nontrivial effects of multi-band geometry since the geometry of the combined bands vanishes for a two-band model, $g_{(12)}^{xx} = \Omega_{(12)}^{xy} = 0$.

In Figs. 2(c), 2(d), 2(f), and 2(h), we show the Berry curvature Ω^{xy} and quantum metric g^{xx} at $k_z = \pi$ for the four-band model C, cf. Appendix B and Table I, with band structure and density of states shown in Fig. 2(e). Here, both d and p sites have the same chemical potential $\mu_d = \mu_p$, which requires a strong d-p coupling H_{dp} in order to obtain the shown band gap. This implies a large orbital mixing between bands. Indeed, the quantum metric g_2^{xx} of band 2 shows additional features at H, see Fig. 2(c), which are not present in the two-band model. As shown in Fig. 2(d), these features are present in the quantum metric $g_{(12)}^{xx}$ of the combined bands 1 and 2. This metric shows no singularity, as expected, because the singularities are compensated by the additional cross-term [40]. In Figs. 2(f) and 2(h) we show the Berry curvature Ω_2^{xy} and $\Omega_{(12)}^{xy}$, respectively. Similarly to the quantum metric, we observe no divergence and find additional contributions at H due to the band gap minimum between band 2 and 3. The four-band model D, see Table I, has only weak d-p coupling and does not show significant additional features compared to the two-band model.

The quantum geometry of an isolated subspace of bands is an interesting property connected to new geometric effects in narrow or flat bands, where the interaction strength exceeds the subspace band width [31, 45, 76, 77]. A key quantity is the integrated quantum metric $\bar{g}_{(12)} \equiv \int \frac{d^3\mathbf{k}}{V} \text{tr} g_{(12)}(\mathbf{k})$ with $V = 16\pi^3/\sqrt{3}$, which can be interpreted as the gauge-invariant part of the Wannier function spread in real space [99]. We find $\bar{g}_{(12)} = 0.26$ and $\bar{g}_{(12)} = 0.03$ for model C and D, respectively. Geometric contributions to observables are, thus, expected to be significantly larger for model C than D.

B. Singular flat bands

Systems with flat bands are promising candidates for phenomena that rely dominantly on quantum geometry. As seen in Fig. 1(h) the two-band model appears to exhibit a flat-band limit with non-vanishing hopping terms, which we identify in the following as a singular flat band.

IV. DISCUSSION

A. Application to pristine copper-doped lead apatite

Our band structures shown in Fig. 1(e), 1(h), 2(e), and 2(g) are able to reproduce most of the key features reported in DFT studies on copper-doped lead apatite that assumed the same regular dopant placement [48–51]. For the two-band model we have identified two parameter sets A and B, see Table I, to capture the band structure for different relative positions of copper and extra oxygen sites [51]. Parameter set B generates the reported almost flat band [48, 51, 101]. Our models show saddle-point Van Hove singularities in all bands at M and L with an energy profile as reported in Ref. [51].

The four-band model with parameter set C, see Table I, is constructed to reproduce the nearly equal distribution of p and d orbitals in the density of states, shown in Fig. 2(e), which was seen in the DFT results [48–51] for bands 1 and 2. The weak d character of bands 3 and 4 in the DFT results cannot be captured by just four bands. Model D corresponds to a weakly coupled four-band model with mixing of d and p orbitals of at most 10%.

Later DFT studies include tight-binding models with parameters reasonably close to ours [102–109]. Note that these models use cubic harmonics, whereas our models correspond to C_3 -symmetric combinations of d and p orbitals, see Appendix A 1. The topology and quantum geometry analyzed in Ref. [102] align with our conclusions.

We emphasize that there is a discrepancy between the assumed pristine material structure in DFT and the materials studied experimentally. Copper-doped lead apatite $\text{Pb}_9\text{Cu}(\text{PO}_4)_6\text{O}$ samples were found to exhibit comparable substitution on both $4f$ and $6h$ Wyckoff positions as well as a clustering of copper [52]. Since the site symmetry of $6h$ only comprises mirror symmetry, no complex representation exists, and therefore a metallic normal state in the absence of interactions, as described in the present paper, is not expected for these samples. The originally proposed unusual resistivity signatures of copper-doped lead apatite (referred to as "LK-99") [110, 111] have been connected to a metal insulator transition [112], which was experimentally related to CuS_2 impurities [52, 102, 113, 114].

B. Further candidate materials

Our results apply to a range of doped variants of established semiconductors. In the rhombohedral van der Waals ferromagnet $\text{Cr}_2\text{Ge}_2\text{Te}_6$ [53, 54] Mn doping increases the carrier density, which coincides with the appearance of a complex representation of the C_3 symmetry, as described in Eq. (1), and is found to improve the thermoelectric figure of merit [55]. Doped monolayers of

	2-band A	2-band B	4-band C	4-band D
μ_d	10	0	250	20
t_{z+}^d	-30	-8	-20	-10
t_{z-}^d	5	2	-3	-2.5
t_{xy+}^d	-5	-4	-20	-5
t_{xy-}^d	30	5	-14	20
\tilde{t}_{xy}^d	15	6	14	10
μ_p			250	500
t_{z+}^p			-70	-200
t_{z-}^p			8	10
t_{xy+}^p			1	10
t_{xy-}^p			-20	80
\tilde{t}_{xy}^p			-14	70
t_{xy}^{dp}			70	50
\tilde{t}_{xy}^{dp}			100	10
t_{xyz}^{dp}			14	10
\tilde{t}_{xyz}^{dp}			14	10

TABLE I. Summary of the used parameters to capture approximately the key features of the DFT results in Refs. [48–51]. All units are meV.

the well-studied semiconductor SiC [56, 57] have in-gap states with bands resembling models A or B at $k_z = 0$, dependent on the chosen dopant [58]. In the 2D dichalcogenide MoS_2 sulfur vacancies act as active centers for hydrogen evolution catalysis [59] and, interestingly, also lead to an impurity band that is qualitatively described by model A [60, 61].

V. CONCLUSION

We discussed how doping-induced states in semiconductors and insulators enable the design of topological and geometrical band structures by choosing a suitable site symmetry. The simplicity yet richness of the constructed two- and four-band model makes them an optimal starting point to study the implications of the discussed nontrivial multiband quantum geometry and singular flat bands. Analogously to the presented example, our method can be applied to other dopant configurations and other doped insulating materials [55, 58, 61, 115], where symmetry-enforced band crossings occur whenever a complex representation exists due a three-, four-, or six-fold rotation symmetry.

ACKNOWLEDGMENTS

The authors thank Alexander Avdoshkin, Zhehao Dai, Tomohiro Soejima, Jan M. Tomczak, and Taige Wang for very stimulating discussions. M.M.H. is funded by the Deutsche Forschungsgemeinschaft (DFG, German Research Foundation) - project number 518238332. J.M. acknowledges support by the German National Academy of Sciences Leopoldina through Grant No. LPDS 2022-06.

Appendix A: Two-band model

1. Symmetry operations

The orbital character of our basis states is introduced by the imposed symmetries. We represent space group $P3$ comprising C_3 rotation and time reversal θ by

$$U_{C_3}^d = \begin{pmatrix} e^{i\frac{2\pi}{3}} & 0 \\ 0 & e^{-i\frac{2\pi}{3}} \end{pmatrix} \text{ and } \theta = \begin{pmatrix} 0 & 1 \\ 1 & 0 \end{pmatrix} K, \quad (\text{A1})$$

respectively, where K refers to the complex conjugation operator. With the above definitions our two-band model in Eq. (1) fulfills

$$(U_{C_3}^d)^\dagger H(\mathbf{k}) U_{C_3}^d = H_d(C_3^{-1}\mathbf{k}), \quad (\text{A2})$$

$$\theta H_d(\mathbf{k}) \theta = H_d(-\mathbf{k}), \quad (\text{A3})$$

where C_3 is the conventional action on spatial coordinates,

$$C_3 = \begin{pmatrix} \cos(2\pi/3) & -\sin(2\pi/3) \\ \sin(2\pi/3) & \cos(2\pi/3) \end{pmatrix}. \quad (\text{A4})$$

This complex representation can model any C_3 -symmetric superposition of orbitals such as d orbitals. If these orbitals are expressed in spherical harmonics $Y_l^m(\theta, \varphi)$, the quantum number m and the eigenvalues λ_{C_3} of threefold rotation fulfill $\lambda_{C_3} = \exp(im2\pi/3)$. Thus, the first (second) component of our basis can represent any superposition of states described by $m = 1, -2$ ($m = -1, 2$). Expressed in cubic harmonics, the complex representation may exhibit contributions from (d_{xz}, d_{yz}) and $(d_{xy}, d_{x^2-y^2})$, which comprise states with $|m| = 1$ and $|m| = 2$, respectively.

2. Possible additional symmetry-allowed hopping terms

In the main text, we have considered only nearest-neighbor hopping terms. To fit the model to a specific band structure, we also provide second- and third-nearest-neighbor hopping terms, with distances in real space $\sqrt{2}$ and $\sqrt{3}$ in units of the lattice constant, respectively. The second-nearest-neighbors that occur are the six vectors shown in Fig. 1(a) combined with a step in the \mathbf{a}_3 direction, which result in a Hamiltonian $\delta H_{11}(\mathbf{k})$ that can be added to $H_{11}(\mathbf{k})$ in Eq. (2). Due to the absence of mirror or additional rotation symmetries in the site symmetry, this corresponds to six generally different terms in $\delta H_{11}(\mathbf{k})$, see Eqs. (A5) and (A6) below. The terms in $\delta H_{11}(\mathbf{k})$ can be used to describe anisotropy along the k_z direction, e.g., the line H₂-K-H similar to t_{z-}^d . But unlike t_{z-}^d the longer range $\delta H_{11}(\mathbf{k})$ acts differently on the axes Γ -A and H₂-K-H. The third-nearest neighbor terms $\delta H_{12}(\mathbf{k})$ are given in Eq. (A7) below,

$$\begin{aligned} \delta H_{11}(\mathbf{k}) = & t_{1,xyz+}^d \left(\cos(\mathbf{k} \cdot (\mathbf{a}_1 + \mathbf{a}_3)) + \cos(\mathbf{k} \cdot (-\mathbf{a}_1 - \mathbf{a}_2 + \mathbf{a}_3)) + \cos(\mathbf{k} \cdot (\mathbf{a}_2 + \mathbf{a}_3)) \right) \\ & + t_{2,xyz+}^d \left(\cos(\mathbf{k} \cdot (\mathbf{a}_1 - \mathbf{a}_3)) + \cos(\mathbf{k} \cdot (-\mathbf{a}_1 - \mathbf{a}_2 - \mathbf{a}_3)) + \cos(\mathbf{k} \cdot (\mathbf{a}_2 - \mathbf{a}_3)) \right) \\ & + t_{1,xyz-}^d \left(\sin(\mathbf{k} \cdot (\mathbf{a}_1 + \mathbf{a}_3)) + \sin(\mathbf{k} \cdot (-\mathbf{a}_1 - \mathbf{a}_2 + \mathbf{a}_3)) + \sin(\mathbf{k} \cdot (\mathbf{a}_2 + \mathbf{a}_3)) \right) \\ & + t_{2,xyz-}^d \left(\sin(\mathbf{k} \cdot (\mathbf{a}_1 + \mathbf{a}_2 + \mathbf{a}_3)) + \sin(\mathbf{k} \cdot (-\mathbf{a}_2 + \mathbf{a}_3)) + \sin(\mathbf{k} \cdot (-\mathbf{a}_1 + \mathbf{a}_3)) \right) \\ & + t_{3,xyz-}^d \left(\sin(\mathbf{k} \cdot (\mathbf{a}_1 - \mathbf{a}_3)) + \sin(\mathbf{k} \cdot (-\mathbf{a}_1 - \mathbf{a}_2 - \mathbf{a}_3)) + \sin(\mathbf{k} \cdot (\mathbf{a}_2 - \mathbf{a}_3)) \right) \\ & + t_{4,xyz-}^d \left(\sin(\mathbf{k} \cdot (\mathbf{a}_1 + \mathbf{a}_2 - \mathbf{a}_3)) + \sin(\mathbf{k} \cdot (-\mathbf{a}_2 - \mathbf{a}_3)) + \sin(\mathbf{k} \cdot (-\mathbf{a}_1 - \mathbf{a}_3)) \right), \end{aligned} \quad (\text{A5})$$

$$\delta H_{22}(\mathbf{k}) = \delta H_{11}(-\mathbf{k}), \quad (\text{A6})$$

$$\delta H_{12}(\mathbf{k}) = \tilde{t}_{1,xy}^d \left(\cos(\mathbf{k} \cdot (2\mathbf{a}_1 + \mathbf{a}_2)) + e^{i\frac{2\pi}{3}} \cos(\mathbf{k} \cdot (-\mathbf{a}_1 - 2\mathbf{a}_2)) + e^{-i\frac{2\pi}{3}} \cos(\mathbf{k} \cdot (-\mathbf{a}_1 + \mathbf{a}_2)) \right)$$

$$+ \tilde{t}_{2,xy}^d \left(\cos(\mathbf{k} \cdot (\mathbf{a}_1 + 2\mathbf{a}_2)) + e^{i\frac{2\pi}{3}} \cos(\mathbf{k} \cdot (\mathbf{a}_1 - \mathbf{a}_2)) + e^{-i\frac{2\pi}{3}} \cos(\mathbf{k} \cdot (-2\mathbf{a}_1 - \mathbf{a}_2)) \right). \quad (\text{A7})$$

3. Real-space version of the tight-binding Hamiltonian

We Fourier transform the tight-binding Hamiltonian for the two-band model in Eq. (1) to real space via

$$\hat{d}_{\mathbf{k},\nu} = \frac{1}{\sqrt{N_c}} \sum_j \hat{d}_{j,\nu} e^{-i\mathbf{k} \cdot (\mathbf{R}_j + \boldsymbol{\rho}_d)} \quad (\text{A8})$$

with lattice vector $\mathbf{R}_{j_1, j_2, j_3} = j_1 \mathbf{a}_1 + j_2 \mathbf{a}_2 + j_3 \mathbf{a}_3$, total number of unit cells N_c , and annihilation operator \hat{d}_ν of the orbital $\nu = 1, 2$ at the unit-cell position $\boldsymbol{\rho}_d = (0, 0, 0)$. We obtain

$$\hat{H} = \hat{H}_{11} + \hat{H}_{22} + \hat{H}_{12} + \hat{H}_{12}^\dagger - \mu_d \sum_j (\hat{d}_{j,1}^\dagger \hat{d}_{j,1} + \hat{d}_{j,2}^\dagger \hat{d}_{j,2}) \quad (\text{A9})$$

with

$$\hat{H}_{11} = \sum_j \left[\frac{t_{xy}^d}{2} \left(\hat{d}_{j+j_1,1}^\dagger \hat{d}_{j,1} + \hat{d}_{j,1}^\dagger \hat{d}_{j+j_1+j_2,1} + \hat{d}_{j+j_2,1}^\dagger \hat{d}_{j,1} \right) + t_z \hat{d}_{j+j_3,1}^\dagger \hat{d}_{j,1} \right] + \text{H.c.}, \quad (\text{A10})$$

$$\hat{H}_{22} = \sum_j \left[\frac{(t_{xy}^d)^*}{2} \left(\hat{d}_{j+j_1,2}^\dagger \hat{d}_{j,2} + \hat{d}_{j,2}^\dagger \hat{d}_{j+j_1+j_2,2} + \hat{d}_{j+j_2,2}^\dagger \hat{d}_{j,2} \right) + (t_z)^* \hat{d}_{j+j_3,2}^\dagger \hat{d}_{j,2} \right] + \text{H.c.}, \quad (\text{A11})$$

with $t_{xy}^d = t_{xy,+}^d + it_{xy,-}^d$ and Hermitian conjugate H.c. as well as

$$\hat{H}_{12} = \sum_j \frac{\tilde{t}_{xy}^d}{2} \left[\left(\hat{d}_{j+j_1,1}^\dagger \hat{d}_{j,2} + \hat{d}_{j,1}^\dagger \hat{d}_{j+j_1,2} \right) + e^{i\frac{2\pi}{3}} \left(\hat{d}_{j+j_1+j_2,1}^\dagger \hat{d}_{j,2} + \hat{d}_{j,1}^\dagger \hat{d}_{j+j_1+j_2,2} \right) + e^{-i\frac{2\pi}{3}} \left(\hat{d}_{j,1}^\dagger \hat{d}_{j+j_2,2} + \hat{d}_{j+j_2,1}^\dagger \hat{d}_{j,2} \right) \right], \quad (\text{A12})$$

and $\hat{H}_{21} = (\hat{H}_{12})^*$.

4. Effect of the parameters on several model properties

We give several relations between basic band structure properties and the five model parameters, the \mathbf{a}_1 - \mathbf{a}_2 -plane hoppings $t_{xy\pm}^d$ and \tilde{t}_{xy}^d and the out-of-plane hoppings $t_{z\pm}^d$. Note that \tilde{t}_{xy}^d is in general complex, whereas the other parameters are real. We focus on the high-symmetry points $\Gamma = (0, 0, 0)$, $M = (\pi, -\pi/\sqrt{3}, 0)$, $K = (4\pi/3, 0, 0)$, $A = (0, 0, \pi)$, $L = (\pi, -\pi/\sqrt{3}, \pi)$, and $H = (4\pi/3, 0, \pi)$.

a. Size of direct band gaps at high-symmetry points and on the Γ - A line

We define the size of the direct band gaps as $\Delta_{\mathbf{k}} = E_+(\mathbf{k}) - E_-(\mathbf{k})$ and obtain

$$\Delta_\Gamma = 0, \quad \Delta_M = 4|\tilde{t}_{xy}^d|, \quad \Delta_K = 3\sqrt{3}|t_{xy-}^d|, \quad (\text{A13})$$

$$\Delta_A = 0, \quad \Delta_L = 4|\tilde{t}_{xy}^d|, \quad \Delta_H = 3\sqrt{3}|t_{xy-}^d|. \quad (\text{A14})$$

We see that $\Delta_\Gamma = \Delta_A = 0$ as expected. Furthermore, $\Delta_M = \Delta_L$ and $\Delta_K = \Delta_H$. The splitting on the symmetry line Γ - A , that is $\mathbf{k} = (0, 0, k_z)$ is given by

$$\Delta_{\Gamma-A} = 2|t_{z-}^d \sin(\mathbf{k} \cdot \mathbf{a}_3)|, \quad (\text{A15})$$

with maximal value $\Delta_{\Gamma-A}^{\max} = 2|t_{z-}^d|$ for $k_z = \pi/2$.

b. Band curvature at Γ and A in various directions

The momentum expansion of the two bands at $\Gamma = (0, 0, 0)$ in direction $\mathbf{v}_{\Gamma-M} = (M - \Gamma)/|M - \Gamma| = (\sqrt{3}/2, -1/2, 0)$ and $\mathbf{v}_{\Gamma-K} = (K - \Gamma)/|K - \Gamma| = (1, 0, 0)$ reads

$$\begin{aligned} E_+(k \mathbf{v}_{\Gamma-M}) &= E_+(k \mathbf{v}_{\Gamma-K}) \\ &= \left(3t_{xy+}^d + t_{z+}^d - \mu_d \right) + \frac{3}{8} \left(|\tilde{t}_{xy}^d| - 2t_{xy+}^d \right) k^2 + \mathcal{O}(k^3), \end{aligned} \quad (\text{A16})$$

$$\begin{aligned} E_-(k \mathbf{v}_{\Gamma-M}) &= E_-(k \mathbf{v}_{\Gamma-K}) \\ &= \left(3t_{xy+}^d + t_{z+}^d - \mu_d \right) - \frac{3}{8} \left(|\tilde{t}_{xy}^d| + 2t_{xy+}^d \right) k^2 + \mathcal{O}(k^3). \end{aligned} \quad (\text{A17})$$

The momentum expansion of the two bands at $A = (0, 0, \pi)$ in direction $\mathbf{v}_{\mathbf{A}-\mathbf{L}} = (L - A)/|L - A| = (\sqrt{3}/2, -1/2, 0)$ and $\mathbf{v}_{\mathbf{A}-\mathbf{H}} = (H - A)/|H - A| = (1, 0, 0)$ reads

$$\begin{aligned} E_+(k \mathbf{v}_{\mathbf{A}-\mathbf{L}}) &= E_+(k \mathbf{v}_{\mathbf{A}-\mathbf{H}}) \\ &= (3t_{xy+}^d - t_{z+}^d - \mu_d) + \frac{3}{8}(|\tilde{t}_{xy}^d| - 2t_{xy+}^d)k^2 + \mathcal{O}(k^3), \end{aligned} \quad (\text{A18})$$

$$\begin{aligned} E_-(k \mathbf{v}_{\mathbf{A}-\mathbf{L}}) &= E_-(k \mathbf{v}_{\mathbf{A}-\mathbf{H}}) \\ &= (3t_{xy+}^d - t_{z+}^d - \mu_d) - \frac{3}{8}(|\tilde{t}_{xy}^d| + 2t_{xy+}^d)k^2 + \mathcal{O}(k^3). \end{aligned} \quad (\text{A19})$$

We read off six different scenarios. If $|\tilde{t}_{xy}^d| = 2|t_{xy+}^d|$ or $|\tilde{t}_{xy}^d| = -2|t_{xy+}^d|$, the upper or the lower band remains flat. We conclude the following trends: (i) E_+ has positive curvature if $|\tilde{t}_{xy}^d| > 2t_{xy+}^d$, (ii) E_+ has negative curvature if $|\tilde{t}_{xy}^d| < 2t_{xy+}^d$, (iii) E_- has positive curvature if $|\tilde{t}_{xy}^d| < -2t_{xy+}^d$, and (iv) E_- has negative curvature if $|\tilde{t}_{xy}^d| > -2t_{xy+}^d$. We see that the trends depend on the relative size of $|\tilde{t}_{xy}^d|$ and $|t_{xy+}^d|$ as well as the sign of t_{xy+}^d . We summarize the result in Table II.

c. Lower-band shift at K and H with respect to Γ

The energy of the lower band at high-symmetry points K and H with respect to Γ is given by

$$E_-(K) - E_-(\Gamma) = -\frac{3\sqrt{3}}{2}|t_{xy-}^d| - \frac{9}{2}t_{xy+}^d, \quad (\text{A20})$$

$$E_-(H) - E_-(\Gamma) = -\frac{3\sqrt{3}}{2}|t_{xy-}^d| - \frac{9}{2}t_{xy+}^d - 2t_{z+}^d. \quad (\text{A21})$$

5. Berry curvature and quantum metric for the two-band model at $k_z = \pi/2$

For the parameter sets A and B, see Table I, we show the Berry curvature and quantum metric at $k_z = \pi/2$ in Fig. 4. Besides the divergence of Berry curvature and quantum metric at the Weyl points, both quantities exhibit larger values for the parameter set A, i.e., the one with the smaller gap on Γ -A. Notably, albeit the localization of the weight in \mathbf{k} space strongly differs between models A and B, as seen when comparing Fig. 4(c) to Fig. 4(d), the integrated values are of the same order of magnitude. Specifically, integrating the metric on the plane shown in Fig. 4 (c)[(d)] yields $\int \frac{d^2\mathbf{k}}{A} g_-^{xx}(\mathbf{k}) = 0.80$ [0.74] with $A = 8\pi^2/\sqrt{3}$. For the Berry curvature the values are identical, because the integral over the plane shown in Fig. 4(a) and 4(b) equals the Chern number of $\nu = -1$.

E_+	E_-	Conditions
\nearrow	\nearrow	$2 t_{xy+}^d > \tilde{t}_{xy}^d $ and $t_{xy+}^d < 0$
\searrow	\searrow	$2 t_{xy+}^d > \tilde{t}_{xy}^d $ and $t_{xy+}^d > 0$
\nearrow	\searrow	$ \tilde{t}_{xy}^d > 2 t_{xy+}^d $

TABLE II. The parameter dependence of the curvature trends at Γ and A in direction M, K and L, H , respectively. \nearrow indicates a positive curvature. \searrow indicates a negative curvature. The missing combination ($\searrow \nearrow$) is inconsistent with the fixed definition of the lower and upper band and, thus, left out.

Appendix B: Four-band model

1. Sublattice hopping in the four-band model

We give the explicit form of the sublattice hopping of the four-band model in Eq. (5). They are

$$H_{dp}(\mathbf{k}) = e^{i\mathbf{k}\cdot(\mathbf{a}_1+2\mathbf{a}_2)/3+z\mathbf{a}_3} \begin{pmatrix} H_{11}^{dp}(\mathbf{k}) & H_{12}^{dp}(\mathbf{k}) \\ H_{21}^{dp}(\mathbf{k}) & H_{22}^{dp}(\mathbf{k}) \end{pmatrix}, \quad (\text{B1})$$

with the 1b Wyckoff position $(\mathbf{a}_1 + 2\mathbf{a}_2)/3 + z\mathbf{a}_3$ and

$$H_{11}^{dp}(\mathbf{k}) = (t_{xy}^{dp} + t_{xyz}^{dp} e^{i\mathbf{k}\cdot\mathbf{a}_3}) \left[1 + e^{-i\mathbf{k}\cdot\mathbf{a}_2} + e^{-i\mathbf{k}\cdot(\mathbf{a}_1+\mathbf{a}_2)} \right], \quad (\text{B2})$$

$$H_{22}^{dp}(\mathbf{k}) = H_{11}^{dp}(-\mathbf{k})^*, \quad (\text{B3})$$

$$H_{12}^{dp}(\mathbf{k}) = (\tilde{t}_{xy}^{dp} + \tilde{t}_{xyz}^{dp} e^{i\mathbf{k}\cdot\mathbf{a}_3}) \times \left[1 + e^{i\frac{2\pi}{3}} e^{-i\mathbf{k}\cdot\mathbf{a}_2} + e^{-i\frac{2\pi}{3}} e^{-i\mathbf{k}\cdot(\mathbf{a}_1+\mathbf{a}_2)} \right], \quad (\text{B4})$$

$$H_{21}^{dp}(\mathbf{k}) = H_{12}^{dp}(-\mathbf{k})^*. \quad (\text{B5})$$

Note that the relative height difference between the 1a and 1b Wyckoff positions, denoted as z in Eq. (B1), does not affect the band structure. For the present paper the exact value of z does not affect the results, because all considered geometric quantities are restricted to derivatives in the k_x - k_y plane.

2. Symmetries and basis convention

The second pair of bands described by $H_p(\mathbf{k})$ obeys by itself the same symmetry representation as $H_d(\mathbf{k})$, but since the 1b Wyckoff position is not invariant under C_3 , the application of C_3 moves the site into a neighboring unit cell. Thus, the unitary representation U_{C_3} contains a factor of $e^{i\mathbf{k}\cdot(\mathbf{a}_1+\mathbf{a}_2)}$. Yet, once represented in the basis convention introduced by the Fourier transform in Eq. (A8), this phase cancels and one finds

$$U_{C_3}^p = \begin{pmatrix} e^{i\frac{2\pi}{3}} & 0 \\ 0 & e^{-i\frac{2\pi}{3}} \end{pmatrix} \quad (\text{B6})$$

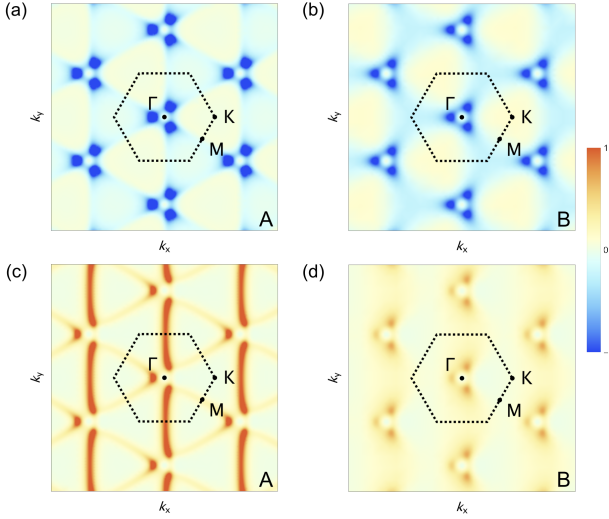


FIG. 4. Berry curvature Ω_-^{xy} [(a),(b)] and quantum metric g_-^{xx} [(c),(d)] at $k_z = \pi/2$ for the parameter sets A and B of the two-band model.

leading to the definition

$$U_{C_3} = \begin{pmatrix} U_{C_3}^d & 0 \\ 0 & U_{C_3}^p \end{pmatrix}, \quad (\text{B7})$$

which is then a symmetry of the four-band model $H_{4 \times 4}(\mathbf{k})$ given in Eq. (5). Time-reversal symmetry is local in real space, and hence is the same for the states corresponding to 1a and 1b Wyckoff positions.

3. Real-space version of the tight-binding Hamiltonian

The tight-binding Hamiltonian defined in Eq. (5) is Fourier transformed to real space via Eq. (A8). The annihilation operators for the d and p orbitals are denoted by \hat{d}_ν and \hat{p}_ν with $\nu = 1, 2$. The d and p orbitals are located at $\boldsymbol{\rho}_d = (0, 0, 0)$ and $\boldsymbol{\rho}_p = (\mathbf{a}_1 + 2\mathbf{a}_2)/3 + z\mathbf{a}_3 = (1/2, 1/2\sqrt{3}, z)$ in the unit cell. The Fourier transform of $H_d(\mathbf{k})$ is already given in Eq. (A9). The Fourier transform of $H_p(\mathbf{k})$ is equivalent to those of $H_d(\mathbf{k})$ with d replaced by p . We give the remaining expressions of $H_{dp}(\mathbf{k})$,

$$\hat{H}_{11}^{dp} = \sum_j \left[t_{xy}^{dp} \left(\hat{d}_{j,1}^\dagger \hat{p}_{j,1} + \hat{d}_{j+j_1+j_2,1}^\dagger \hat{p}_{j,1} + \hat{d}_{j+j_2,1}^\dagger \hat{p}_{j,1} \right) + t_{xyz}^{dp} \left(\hat{d}_{j,1}^\dagger \hat{p}_{j+j_3,1} + \hat{d}_{j+j_1+j_2,1}^\dagger \hat{p}_{j+j_3,1} + \hat{d}_{j+j_2,1}^\dagger \hat{p}_{j+j_3,1} \right) \right], \quad (\text{B8})$$

$$\hat{H}_{22}^{dp} = \sum_j \left[(t_{xy}^{dp})^* \left(\hat{d}_{j,2}^\dagger \hat{p}_{j,2} + \hat{d}_{j+j_1+j_2,2}^\dagger \hat{p}_{j,2} + \hat{d}_{j+j_2,2}^\dagger \hat{p}_{j,2} \right) \right.$$

$$\left. + (t_{xyz}^{dp})^* \left(\hat{d}_{j,2}^\dagger \hat{p}_{j+j_3,2} + \hat{d}_{j+j_1+j_2,2}^\dagger \hat{p}_{j+j_3,2} + \hat{d}_{j+j_2,2}^\dagger \hat{p}_{j+j_3,2} \right) \right], \quad (\text{B9})$$

$$\hat{H}_{12}^{dp} = \sum_j \left[\tilde{t}_{xy}^{dp} \left(\hat{d}_{j,1}^\dagger \hat{p}_{j,2} + e^{i2\pi/3} \hat{d}_{j+j_2,1}^\dagger \hat{p}_{j,2} + e^{-i2\pi/3} \hat{d}_{j+j_1+j_2,1}^\dagger \hat{p}_{j,2} \right) + \tilde{t}_{xyz}^{dp} \left(\hat{d}_{j,1}^\dagger \hat{p}_{j+j_3,2} + e^{i2\pi/3} \hat{d}_{j+j_2,1}^\dagger \hat{p}_{j+j_3,2} + e^{-i2\pi/3} \hat{d}_{j+j_1+j_2,1}^\dagger \hat{p}_{j+j_3,2} \right) \right], \quad (\text{B10})$$

$$\text{and } \hat{H}_{21}^{dp} = (\hat{H}_{12}^{dp})^\dagger.$$

Appendix C: Flat-bands within the two-band model

The eigenvector of the lower band of a generic two-band model reads

$$\mathbf{v}_-(\mathbf{k}) = \frac{1}{\alpha_{\mathbf{k}}} \begin{pmatrix} d_z(\mathbf{k}) - d(\mathbf{k}) \\ d_x(\mathbf{k}) + id_y(\mathbf{k}) \end{pmatrix}. \quad (\text{C1})$$

with normalization $\alpha_{\mathbf{k}} = \sqrt{2} \sqrt{d(\mathbf{k})^2 - d_z(\mathbf{k})d(\mathbf{k})}$, which leads to Eq. (10) after inserting the flat-band condition. Considering the Hamiltonian defined in Eq. (1), we construct

$$d_0(\mathbf{k}) = \frac{1}{2} (H_{11}(\mathbf{k}) + H_{22}(\mathbf{k})), \quad (\text{C2})$$

$$d_x(\mathbf{k}) = \frac{1}{2} (H_{12}(\mathbf{k}) + H_{21}(\mathbf{k})), \quad (\text{C3})$$

$$d_y(\mathbf{k}) = \frac{i}{2} (H_{12}(\mathbf{k}) - H_{21}(\mathbf{k})), \quad (\text{C4})$$

$$d_z(\mathbf{k}) = \frac{1}{2} (H_{11}(\mathbf{k}) - H_{22}(\mathbf{k})). \quad (\text{C5})$$

We are interested in a flat band in the x - y plane and fix $k_z = 0$. Following the procedure as described in Sec. III B 1, we obtain four sets of flat-band conditions different in the relative sign only,

$$t_{xy+}^d = -\frac{1}{2} |\tilde{t}_{xy}^d|, \quad t_{xy-}^d = -\frac{\sqrt{3}}{2} |\tilde{t}_{xy}^d|, \quad c_0 = \frac{3}{2} |\tilde{t}_{xy}^d| - t_{z+}^d + \mu_d, \quad (\text{C6})$$

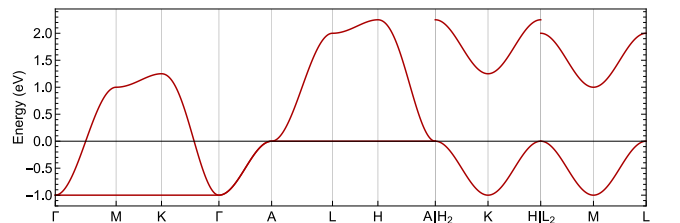


FIG. 5. Band structure fulfilling the flat-band conditions.

$$t_{xy+}^d = -\frac{1}{2}|\tilde{t}_{xy}^d|, t_{xy-}^d = \frac{\sqrt{3}}{2}|\tilde{t}_{xy}^d|, c_0 = \frac{3}{2}|\tilde{t}_{xy}^d| - t_{z+}^d + \mu_d, \quad (\text{C7})$$

$$t_{xy+}^d = \frac{1}{2}|\tilde{t}_{xy}^d|, t_{xy-}^d = -\frac{\sqrt{3}}{2}|\tilde{t}_{xy}^d|, c_0 = -\frac{3}{2}|\tilde{t}_{xy}^d| - t_{z+}^d + \mu_d, \quad (\text{C8})$$

$$t_{xy+}^d = \frac{1}{2}|\tilde{t}_{xy}^d|, t_{xy-}^d = \frac{\sqrt{3}}{2}|\tilde{t}_{xy}^d|, c_0 = -\frac{3}{2}|\tilde{t}_{xy}^d| - t_{z+}^d + \mu_d. \quad (\text{C9})$$

The dispersion in the x - y plane remains flat for any k_z for arbitrary t_{z+}^d . A finite t_{z-}^d gaps the quadratic band touching at $k_x = k_y = 0$ for any $k_z \neq 0, \pi$ and breaks the flat-band conditions leading to a dispersive lower band in the x - y plane. Using Eq. (C6), the parameters discussed in Sec. III B 2 are chosen such that the flat lower band has energy $E_-(\mathbf{k}) = -1$ for $k_z = 0$ and $E_-(\mathbf{k}) = 0$ for $k_z = \pi$ with band gap $E_+(\mathbf{k}) - E_-(\mathbf{k}) = 2$ at momentum $M = (\pi, -\pi/\sqrt{3}, 0)$. The Hamiltonian for $t_{z-}^d = 0$ explicitly reads

$$d_0(\mathbf{k}) = \frac{1}{4} \left(1 - \cos((\mathbf{a}_1 + \mathbf{a}_2) \cdot \mathbf{k}) - \cos(\mathbf{a}_1 \cdot \mathbf{k}) - \cos(\mathbf{a}_2 \cdot \mathbf{k}) - 2 \cos(\mathbf{a}_3 \cdot \mathbf{k}) \right), \quad (\text{C10})$$

$$d_x(\mathbf{k}) = \frac{1}{4} \left(\cos((\mathbf{a}_1 + \mathbf{a}_2) \cdot \mathbf{k}) - 2 \cos(\mathbf{a}_1 \cdot \mathbf{k}) + \cos(\mathbf{a}_2 \cdot \mathbf{k}) \right), \quad (\text{C11})$$

$$d_y(\mathbf{k}) = \frac{\sqrt{3}}{4} \left(\cos((\mathbf{a}_1 + \mathbf{a}_2) \cdot \mathbf{k}) - \cos(\mathbf{a}_2 \cdot \mathbf{k}) \right), \quad (\text{C12})$$

$$d_z(\mathbf{k}) = \frac{\sqrt{3}}{4} \left(\sin((\mathbf{a}_1 + \mathbf{a}_2) \cdot \mathbf{k}) - \sin(\mathbf{a}_1 \cdot \mathbf{k}) - \sin(\mathbf{a}_2 \cdot \mathbf{k}) \right). \quad (\text{C13})$$

The dispersion is shown in Fig. 5. The normalization of the CLS in Eq. (13) is

$$\alpha_{\mathbf{k}}^2 = 2 \left(-3 + \cos((\mathbf{a}_1 + \mathbf{a}_2) \cdot \mathbf{k}) + \cos(\mathbf{a}_1 \cdot \mathbf{k}) + \cos(\mathbf{a}_2 \cdot \mathbf{k}) \right) \times \left(-3 + \cos((\mathbf{a}_1 + \mathbf{a}_2) \cdot \mathbf{k}) + \cos(\mathbf{a}_1 \cdot \mathbf{k}) + \cos(\mathbf{a}_2 \cdot \mathbf{k}) - \sqrt{3} \left(\sin(\mathbf{a}_1 \cdot \mathbf{k}) + \sin(\mathbf{a}_2 \cdot \mathbf{k}) - \sin((\mathbf{a}_1 + \mathbf{a}_2) \cdot \mathbf{k}) \right) \right), \quad (\text{C14})$$

which vanishes at $\Gamma = (0, 0, 0)$.

-
- [1] M. Z. Hasan and C. L. Kane, Colloquium: Topological insulators, *Reviews of modern physics* **82**, 3045 (2010).
- [2] C.-K. Chiu, J. C. Y. Teo, A. P. Schnyder, and S. Ryu, Classification of topological quantum matter with symmetries, *Rev. Mod. Phys.* **88**, 035005 (2016).
- [3] A. Burkov, Topological semimetals, *Nature materials* **15**, 1145 (2016).
- [4] Y.-H. Chan, C.-K. Chiu, M. Y. Chou, and A. P. Schnyder, Ca_3P_2 and other topological semimetals with line nodes and drumhead surface states, *Phys. Rev. B* **93**, 205132 (2016).
- [5] A. Bernevig, H. Weng, Z. Fang, and X. Dai, Recent progress in the study of topological semimetals, *Journal of the Physical Society of Japan* **87**, 041001 (2018).
- [6] M. Vergniory, L. Elcoro, C. Felser, N. Regnault, B. A. Bernevig, and Z. Wang, A complete catalogue of high-quality topological materials, *Nature* **566**, 480 (2019).
- [7] K. Choudhary, K. F. Garrity, and F. Tavazza, High-throughput discovery of topologically non-trivial materials using spin-orbit spillage, *Scientific reports* **9**, 8534 (2019).
- [8] Y. Xu, L. Elcoro, Z.-D. Song, B. J. Wieder, M. Vergniory, N. Regnault, Y. Chen, C. Felser, and B. A. Bernevig, High-throughput calculations of magnetic topological materials, *Nature* **586**, 702 (2020).
- [9] T. Yu, R. Arita, and M. Hirayama, Interstitial-electron-induced topological molecular crystals, *Adv. Phys. Research* **2**, 2200041 (2023).
- [10] J.-Y. Noh, H. Kim, and Y.-S. Kim, Stability and electronic structures of native defects in single-layer MoS_2 , *Phys. Rev. B* **89**, 205417 (2014).
- [11] D. J. Trainer, J. Nieminen, F. Bobba, B. Wang, X. Xi, A. Bansil, and M. Iavarone, Visualization of defect induced in-gap states in monolayer MoS_2 , *npj 2D Mater. Appl.* **6**, 13 (2022).
- [12] P. A. Schultz, Theory of defect levels and the “band gap problem” in silicon, *Phys. Rev. Lett.* **96**, 246401 (2006).
- [13] H. Kim, C.-g. Oh, and J.-W. Rhim, General construction scheme for geometrically nontrivial flat band models, *Commun Phys* **6**, 305 (2023).
- [14] S. Nishino, M. Goda, and K. Kusakabe, Flat bands of a tight-binding electronic system with hexagonal structure, *Journal of the Physical Society of Japan* **72**, 2015 (2003).
- [15] Z. Liu, M. Li, Q. Wang, G. Wang, C. Wen, K. Jiang, X. Lu, S. Yan, Y. Huang, D. Shen, *et al.*, Orbital-selective dirac fermions and extremely flat bands in frustrated kagome-lattice metal CoSn , *Nature communications* **11**, 4002 (2020).
- [16] R. Bistritzer and A. H. MacDonald, Moire bands in twisted double-layer graphene, *Proceedings of the National Academy of Sciences* **108**, 12233 (2011).
- [17] Y. Cao, V. Fatemi, A. Demir, S. Fang, S. L. Tomarken, J. Y. Luo, J. D. Sanchez-Yamagishi, K. Watanabe, T. Taniguchi, E. Kaxiras, R. C. Ashoori, and P. Jarillo-Herrero, Correlated insulator behaviour at half-filling in magic-angle graphene superlattices, *Nature* **556**, 80 (2018).
- [18] Y. Cao, V. Fatemi, S. Fang, K. Watanabe, T. Taniguchi, E. Kaxiras, and P. Jarillo-Herrero, Unconventional superconductivity in magic-angle graphene superlattices,

- Nature* **556**, 43 (2018).
- [19] V. o. T. Phong and E. J. Mele, Quantum geometric oscillations in two-dimensional flat-band solids, *Phys. Rev. Lett.* **130**, 266601 (2023).
- [20] K. Sun, Z. Gu, H. Katsura, and S. Das Sarma, Nearly flatbands with nontrivial topology, *Phys. Rev. Lett.* **106**, 236803 (2011).
- [21] M. Han, H. Inoue, S. Fang, C. John, L. Ye, M. K. Chan, D. Graf, T. Suzuki, M. P. Ghimire, W. J. Cho, E. Kaxiras, and J. G. Checkelsky, Evidence of two-dimensional flat band at the surface of antiferromagnetic kagome metal FeSn, *Nature Communications* **12**, 5345 (2021).
- [22] L. Zheng, L. Feng, and W. Yong-Shi, Exotic electronic states in the world of flat bands: From theory to material, *Chinese Physics B* **23**, 077308 (2014).
- [23] P. M. Neves, J. P. Wakefield, S. Fang, H. Nguyen, L. Ye, and J. G. Checkelsky, Crystal net catalog of model flat band materials (2023), [arXiv:2303.02524](https://arxiv.org/abs/2303.02524) [[cond-mat.mtrl-sci](https://arxiv.org/abs/2303.02524)].
- [24] H. Tian, X. Gao, Y. Zhang, S. Che, T. Xu, P. Cheung, K. Watanabe, T. Taniguchi, M. Randeria, F. Zhang, C. N. Lau, and M. W. Bockrath, Evidence for Dirac flat band superconductivity enabled by quantum geometry, *Nature* **614**, 440 (2023).
- [25] M. Kang, S. Fang, L. Ye, H. C. Po, J. Denlinger, C. Jozwiak, A. Bostwick, E. Rotenberg, E. Kaxiras, J. G. Checkelsky, and R. Comin, Topological flat bands in frustrated kagome lattice CoSn, *Nature Communications* **11**, 4004 (2020).
- [26] D. Kim and F. Liu, Realization of flat bands by lattice intercalation in kagome metals, *Phys. Rev. B* **107**, 205130 (2023).
- [27] A. Lau, T. Hyart, C. Autieri, A. Chen, and D. I. Pikulin, Designing three-dimensional flat bands in nodal-line semimetals, *Phys. Rev. X* **11**, 031017 (2021).
- [28] I. Dutta and K. Saha, Non-trivial flat bands in three dimensions (2023), [arXiv:2305.09616](https://arxiv.org/abs/2305.09616) [[cond-mat.mes-hall](https://arxiv.org/abs/2305.09616)].
- [29] J. Liu, C. Danieli, J. Zhong, and R. A. Römer, Unconventional delocalization in a family of three-dimensional lieb lattices, *Phys. Rev. B* **106**, 214204 (2022).
- [30] J. P. Provost and G. Vallee, Riemannian Structure on Manifolds of Quantum States, *Communications in Mathematical Physics* **76**, 289 (1980).
- [31] S. Peotta and P. Törmä, Superfluidity in topologically nontrivial flat bands, *Nature Communications* **6**, 8944 (2015).
- [32] T. Holder, D. Kaplan, and B. Yan, Consequences of time-reversal-symmetry breaking in the light-matter interaction: Berry curvature, quantum metric, and diabatic motion, *Phys. Rev. Research* **2**, 033100 (2020).
- [33] J. Mitscherling, Longitudinal and anomalous Hall conductivity of a general two-band model, *Phys. Rev. B* **102**, 165151 (2020).
- [34] I. Komissarov, T. Holder, and R. Queiroz, The quantum geometric origin of capacitance in insulators (2023), [arXiv:2306.08035](https://arxiv.org/abs/2306.08035) [[cond-mat.mes-hall](https://arxiv.org/abs/2306.08035)].
- [35] T. Morimoto, S. Kitamura, and N. Nagaosa, Geometric aspects of nonlinear and nonequilibrium phenomena, *Journal of the Physical Society of Japan* **92**, 072001 (2023).
- [36] J. Ahn, G.-Y. Guo, and N. Nagaosa, Low-frequency divergence and quantum geometry of the bulk photovoltaic effect in topological semimetals, *Phys. Rev. X* **10**, 041041 (2020).
- [37] J. Ahn, G.-Y. Guo, N. Nagaosa, and A. Vishwanath, Riemannian geometry of resonant optical responses, *Nature Physics* **18**, 290 (2022).
- [38] W. T. Tai and M. Claassen, Quantum-geometric light-matter coupling in correlated quantum materials (2023), [arXiv:2303.01597](https://arxiv.org/abs/2303.01597) [[cond-mat.str-el](https://arxiv.org/abs/2303.01597)].
- [39] A. Graf and F. Piéchon, Berry curvature and quantum metric in n -band systems: An eigenprojector approach, *Phys. Rev. B* **104**, 085114 (2021).
- [40] B. Mera and J. Mitscherling, Nontrivial quantum geometry of degenerate flat bands, *Phys. Rev. B* **106**, 165133 (2022).
- [41] A. Avdoshkin and F. K. Popov, Extrinsic geometry of quantum states, *Physical Review B* **107**, 10.1103/physrevb.107.245136 (2023).
- [42] J. Herzog-Arbeitman, A. Chew, K.-E. Huhtinen, P. Törmä, and B. A. Bernevig, Many-Body Superconductivity in Topological Flat Bands, [arXiv:2209.00007](https://arxiv.org/abs/2209.00007) [[cond-mat.str-el](https://arxiv.org/abs/2209.00007)].
- [43] J. Herzog-Arbeitman, V. Peri, F. Schindler, S. D. Huber, and B. A. Bernevig, Superfluid Weight Bounds from Symmetry and Quantum Geometry in Flat Bands, *Phys. Rev. Lett.* **128**, 087002 (2022).
- [44] G. Bouzerar and D. Mayou, Quantum transport in flat bands and supermetallicity, *Phys. Rev. B* **103**, 075415 (2021).
- [45] J. Mitscherling and T. Holder, Bound on resistivity in flat-band materials due to the quantum metric, *Phys. Rev. B* **105**, 085154 (2022).
- [46] B. Hetényi and P. Lévy, Fluctuations, uncertainty relations, and the geometry of quantum state manifolds, *Phys. Rev. A* **108**, 032218 (2023).
- [47] A. Bouhon, A. Timmel, and R.-J. Slager, Quantum geometry beyond projective single bands (2023), [arXiv:2303.02180](https://arxiv.org/abs/2303.02180) [[cond-mat.mes-hall](https://arxiv.org/abs/2303.02180)].
- [48] S. M. Griffin, Origin of correlated isolated flat bands in copper-substituted lead phosphate apatite (2023), [arXiv:2307.16892](https://arxiv.org/abs/2307.16892) [[cond-mat.supr-con](https://arxiv.org/abs/2307.16892)].
- [49] R. Kurlito, S. Lany, D. Pashov, S. Acharya, M. van Schilfgaarde, and D. S. Dessau, Pb-apatite framework as a generator of novel flat-band CuO based physics, including possible room temperature superconductivity (2023), [arXiv:2308.00698](https://arxiv.org/abs/2308.00698) [[cond-mat.supr-con](https://arxiv.org/abs/2308.00698)].
- [50] L. Si and K. Held, Electronic structure of the putative room-temperature superconductor $\text{Pb}_9\text{Cu}(\text{PO}_4)_6\text{O}$ (2023), [arXiv:2308.00676](https://arxiv.org/abs/2308.00676) [[cond-mat.supr-con](https://arxiv.org/abs/2308.00676)].
- [51] J. Lai, J. Li, P. Liu, Y. Sun, and X.-Q. Chen, First-principles study on the electronic structure $\text{Pb}_{10-x}\text{Cu}_x(\text{PO}_4)_6\text{O}$ ($x = 0, 1$), *Journal of Materials Science & Technology* **171**, 66 (2024).
- [52] P. Puphal, M. Y. P. Akbar, M. Hepting, E. Goering, M. Isobe, A. A. Nugroho, and B. Keimer, Single crystal synthesis, structure, and magnetism of $\text{Pb}_{10-x}\text{Cu}_x(\text{PO}_4)_6\text{O}$, *APL Materials* **11**, 101128 (2023).
- [53] C. Gong, L. Li, Z. Li, H. Ji, A. Stern, Y. Xia, T. Cao, W. Bao, C. Wang, Y. Wang, *et al.*, Discovery of intrinsic ferromagnetism in two-dimensional van der Waals crystals, *Nature* **546**, 265 (2017).
- [54] I. A. Verzhbitskiy, H. Kurebayashi, H. Cheng, J. Zhou, S. Khan, Y. P. Feng, and G. Eda, Controlling the magnetic anisotropy in $\text{Cr}_2\text{Ge}_2\text{Te}_6$ by electrostatic gating, *Nature Electronics* **3**, 460 (2020).
- [55] X. Tang, D. Fan, K. Peng, D. Yang, L. Guo, X. Lu, J. Dai, G. Wang, H. Liu, and X. Zhou, Dopant in-

- duced impurity bands and carrier concentration control for thermoelectric enhancement in p-type $\text{Cr}_2\text{Ge}_2\text{Te}_6$, *Chemistry of Materials* **29**, 7401 (2017).
- [56] T. Kimoto and J. A. Cooper, *Fundamentals of silicon carbide technology: growth, characterization, devices and applications* (John Wiley & Sons, 2014).
- [57] F. Roccaforte, P. Fiorenza, M. Vivona, G. Greco, and F. Giannazzo, Selective doping in silicon carbide power devices, *Materials* **14**, 3923 (2021).
- [58] M. Luo and Y. Shen, Magnetic properties of SiC monolayer with different nonmagnetic metal dopants, *Journal of Superconductivity and Novel Magnetism* **31**, 3277 (2018).
- [59] Y. Cao, Roadmap and direction toward high-performance MoS_2 hydrogen evolution catalysts, *ACS nano* **15**, 11014 (2021).
- [60] S. W. Han, G.-B. Cha, K. Kim, and S. C. Hong, Hydrogen interaction with a sulfur-vacancy-induced occupied defect state in the electronic band structure of MoS_2 , *Physical Chemistry Chemical Physics* **21**, 15302 (2019).
- [61] L. Loh, Z. Zhang, M. Bosman, and G. Eda, Substitutional doping in 2d transition metal dichalcogenides, *Nano Research* **14**, 1668 (2021).
- [62] O. Derzhko, J. Richter, and M. Maksymenko, Strongly correlated flat-band systems: The route from Heisenberg spins to Hubbard electrons, *International Journal of Modern Physics B* **29**, 1530007 (2015).
- [63] A. Mielke, Ferromagnetic ground states for the Hubbard model on line graphs, *Journal of Physics A: Mathematical and General* **24**, L73 (1991).
- [64] A. Mielke, Ferromagnetism in the Hubbard model on line graphs and further considerations, *Journal of Physics A: Mathematical and General* **24**, 3311 (1991).
- [65] H. Tasaki, From Nagaoka's Ferromagnetism to Flat-Band Ferromagnetism and Beyond: An Introduction to Ferromagnetism in the Hubbard Model, *Progress of Theoretical Physics* **99**, 489 (1998).
- [66] D. L. Bergman, C. Wu, and L. Balents, Band touching from real-space topology in frustrated hopping models, *Phys. Rev. B* **78**, 125104 (2008).
- [67] V. A. J. Pyykkönen, S. Peotta, P. Fabritius, J. Mohan, T. Esslinger, and P. Törmä, Flat-band transport and Josephson effect through a finite-size sawtooth lattice, *Phys. Rev. B* **103**, 144519 (2021).
- [68] K. Kobayashi, M. Okumura, S. Yamada, M. Machida, and H. Aoki, Superconductivity in repulsively interacting fermions on a diamond chain: Flat-band-induced pairing, *Phys. Rev. B* **94**, 214501 (2016).
- [69] W. Maimaiti, A. Andreanov, H. C. Park, O. Gendelman, and S. Flach, Compact localized states and flat-band generators in one dimension, *Phys. Rev. B* **95**, 115135 (2017).
- [70] W. Häusler, Flat-band conductivity properties at long-range Coulomb interactions, *Phys. Rev. B* **91**, 041102 (2015).
- [71] M. Creutz, End states, ladder compounds, and domain-wall fermions, *Phys. Rev. Lett.* **83**, 2636 (1999).
- [72] T. Bilitewski and R. Moessner, Disordered flat bands on the kagome lattice, *Phys. Rev. B* **98**, 235109 (2018).
- [73] J. D. Bodyfelt, D. Leykam, C. Danieli, X. Yu, and S. Flach, Flatbands under correlated perturbations, *Phys. Rev. Lett.* **113**, 236403 (2014).
- [74] S. M. Chan, B. Grémaud, and G. G. Batrouni, Pairing and superconductivity in quasi-one-dimensional flat-band systems: Creutz and sawtooth lattices, *Phys. Rev. B* **105**, 024502 (2022).
- [75] Y.-P. Lin, C. Liu, and J. E. Moore, Complex magnetic and spatial symmetry breaking from correlations in kagome flat bands (2023), [arXiv:2307.11810](https://arxiv.org/abs/2307.11810) [cond-mat.str-el].
- [76] D. Mao and D. Chowdhury, Diamagnetic response and phase stiffness for interacting isolated narrow bands, *Proceedings of the National Academy of Sciences* **120**, e2217816120 (2023).
- [77] J. S. Hofmann, E. Berg, and D. Chowdhury, Superconductivity, pseudogap, and phase separation in topological flat bands, *Phys. Rev. B* **102**, 201112 (2020).
- [78] V. Peri, Z.-D. Song, B. A. Bernevig, and S. D. Huber, Fragile topology and flat-band superconductivity in the strong-coupling regime, *Phys. Rev. Lett.* **126**, 027002 (2021).
- [79] N. Roy, A. Ramachandran, and A. Sharma, Interplay of disorder and interactions in a flat-band supporting diamond chain, *Phys. Rev. Research* **2**, 043395 (2020).
- [80] S. Sayyad, E. W. Huang, M. Kitatani, M.-S. Vaezi, Z. Nussinov, A. Vaezi, and H. Aoki, Pairing and non-fermi liquid behavior in partially flat-band systems: Beyond nesting physics, *Phys. Rev. B* **101**, 014501 (2020).
- [81] Y. Hwang, J. Jung, J.-W. Rhim, and B.-J. Yang, Wavefunction geometry of band crossing points in two dimensions, *Phys. Rev. B* **103**, L241102 (2021).
- [82] G. Jiang and Y. Barlas, Pair density waves from local band geometry, *Phys. Rev. Lett.* **131**, 016002 (2023).
- [83] T. Kitamura, A. Daido, and Y. Yanase, Spin-triplet superconductivity from quantum-geometry-induced ferromagnetic fluctuation (2023), [arXiv:2304.11536](https://arxiv.org/abs/2304.11536) [cond-mat.supr-con].
- [84] S. Sayyad, M. Kitatani, A. Vaezi, and H. Aoki, Nematicity-enhanced superconductivity in systems with a non-Fermi liquid behavior, *Journal of Physics: Condensed Matter* **35**, 245605 (2023).
- [85] P. Müller, J. Richter, and O. Derzhko, Hubbard models with nearly flat bands: Ground-state ferromagnetism driven by kinetic energy, *Phys. Rev. B* **93**, 144418 (2016).
- [86] R. Mondaini, G. G. Batrouni, and B. Grémaud, Pairing and superconductivity in the flat band: Creutz lattice, *Phys. Rev. B* **98**, 155142 (2018).
- [87] I. Mahyaeh, T. Köhler, A. M. Black-Schaffer, and A. Kantian, Superconducting pairing from repulsive interactions of fermions in a flat-band system, *Phys. Rev. B* **106**, 125155 (2022).
- [88] S. Brückner, G. Lusvardi, L. Menabue, and M. Saladini, Crystal structure of lead hydroxyapatite from powder x-ray diffraction data, *Inorganica Chimica Acta* **236**, 209 (1995).
- [89] S. V. Krivovichev and P. C. Burns, Crystal chemistry of lead oxide phosphates: crystal structures of $\text{Pb}_4\text{O}(\text{PO}_4)_2$, $\text{Pb}_8\text{O}_5(\text{PO}_4)_2$ and $\text{Pb}_{10}(\text{PO}_4)_6\text{O}$, *Zeitschrift für Kristallographie-Crystalline Materials* **218**, 357 (2003).
- [90] B. Bradlyn, L. Elcoro, J. Cano, M. G. Vergniory, Z. Wang, C. Felser, M. I. Aroyo, and B. A. Bernevig, Topological quantum chemistry, *Nature* **547**, 298 (2017).
- [91] J. Zhang, Y.-H. Chan, C.-K. Chiu, M. G. Vergniory, L. M. Schoop, and A. P. Schnyder, Topological band crossings in hexagonal materials, *Physical Review Materials* **2**, 074201 (2018).

- [92] B.-J. Yang, T. A. Bojesen, T. Morimoto, and A. Furusaki, Topological semimetals protected by off-centered symmetries in nonsymmorphic crystals, *Physical Review B* **95**, 075135 (2017).
- [93] M. A. Wilde, M. Dodenhöft, A. Niedermayr, A. Bauer, M. M. Hirschmann, K. Alpin, A. P. Schnyder, and C. Pfleiderer, Symmetry-enforced topological nodal planes at the fermi surface of a chiral magnet, *Nature* **594**, 374 (2021).
- [94] Y. Tokura and N. Nagaosa, Nonreciprocal responses from non-centrosymmetric quantum materials, *Nature communications* **9**, 3740 (2018).
- [95] G. Chang, B. J. Wieder, F. Schindler, D. S. Sanchez, I. Belopolski, S.-M. Huang, B. Singh, D. Wu, T.-R. Chang, T. Neupert, *et al.*, Topological quantum properties of chiral crystals, *Nature materials* **17**, 978 (2018).
- [96] S. S. Tsirkin, I. Souza, and D. Vanderbilt, Composite Weyl nodes stabilized by screw symmetry with and without time-reversal invariance, *Physical Review B* **96**, 045102 (2017).
- [97] K. Alpin, M. M. Hirschmann, N. Heinsdorf, A. Leonhardt, W. Y. Yau, X. Wu, and A. P. Schnyder, Fundamental laws of chiral band crossings: Local constraints, global constraints, and topological phase diagrams, *Phys. Rev. Res.* **5**, 043165 (2023).
- [98] T. Fukui, Y. Hatsugai, and H. Suzuki, Chern numbers in discretized Brillouin zone: efficient method of computing (spin) Hall conductances, *Journal of the Physical Society of Japan* **74**, 1674 (2005).
- [99] N. Marzari, A. A. Mostofi, J. R. Yates, I. Souza, and D. Vanderbilt, Maximally localized Wannier functions: Theory and applications, *Rev. Mod. Phys.* **84**, 1419 (2012).
- [100] J.-W. Rhim and B.-J. Yang, Classification of flat bands according to the band-crossing singularity of Bloch wave functions, *Phys. Rev. B* **99**, 045107 (2019).
- [101] O. Tavakol and T. Scaffidi, Minimal model for the flat bands in copper-substituted lead phosphate apatite (2023), [arXiv:2308.01315 \[cond-mat.supr-con\]](https://arxiv.org/abs/2308.01315).
- [102] Y. Jiang, S. B. Lee, J. Herzog-Arbeitman, J. Yu, X. Feng, H. Hu, D. Calugaru, P. S. Brodale, E. L. Gormley, M. G. Vergniory, C. Felser, S. Blanco-Canosa, C. H. Hendon, L. M. Schoop, and B. A. Bernevig, $\text{Pb}_9\text{Cu}(\text{PO}_4)_6(\text{OH})_2$: Phonon bands, localized flat-band magnetism, models, and chemical analysis, *Phys. Rev. B* **108**, 235127 (2023).
- [103] M. Fidrysiak, A. P. Kadzielawa, and J. Spalek, High Temperature Superconductivity with Strong Correlations and Disorder: Possible Relevance to Cu-doped Apatite (2023), [arXiv:2308.03948 \[cond-mat.supr-con\]](https://arxiv.org/abs/2308.03948).
- [104] L. Si, M. Wallerberger, A. Smolyanyuk, S. di Cataldo, J. M. Tomczak, and K. Held, $\text{Pb}_{10-x}\text{Cu}_x(\text{PO}_4)_6\text{O}$: a Mott or charge transfer insulator in need of further doping for (super)conductivity, *J. Phys.: Condens. Matter* **36**, 065601 (2024).
- [105] N. Mao, N. Peshchenko, and Y. Zhang, Wannier functions, minimal model and charge transfer in $\text{Pb}_9\text{CuP}_6\text{O}_{25}$ (2023), [arXiv:2308.05528 \[cond-mat.supr-con\]](https://arxiv.org/abs/2308.05528).
- [106] C. Yue, V. Christiansson, and P. Werner, Correlated electronic structure of $\text{Pb}_{10-x}\text{Cu}_x(\text{PO}_4)_6\text{O}$ (2023), [arXiv:2308.04976 \[cond-mat.str-el\]](https://arxiv.org/abs/2308.04976).
- [107] H. Bai, L. Gao, and C. Zeng, Semiconductivity induced by spin-orbit coupling in $\text{Pb}_9\text{Cu}(\text{PO}_4)_6\text{O}$, *Sci Rep* **13**, 21085 (2023).
- [108] D. M. Korotin, D. Y. Novoselov, A. O. Shorikov, V. I. Anisimov, and A. R. Oganov, Electronic correlations in the ultranarrow energy band compound $\text{Pb}_9\text{Cu}(\text{PO}_4)_6\text{O}$: A DFT + DMFT study, *Phys. Rev. B* **108**, L241111 (2023).
- [109] N. Witt, L. Si, J. M. Tomczak, K. Held, and T. Wehling, No superconductivity in $\text{Pb}_9\text{Cu}_1(\text{PO}_4)_6\text{O}$ found in orbital and spin fluctuation exchange calculations (2023), [arXiv:2308.07261 \[cond-mat.supr-con\]](https://arxiv.org/abs/2308.07261).
- [110] S. Lee, J.-H. Kim, and Y.-W. Kwon, The first room-temperature ambient-pressure superconductor (2023), [arXiv:2307.12008 \[cond-mat.supr-con\]](https://arxiv.org/abs/2307.12008).
- [111] S. Lee, J. Kim, H.-T. Kim, S. Im, S. An, and K. H. Auh, Superconductor $\text{Pb}_{10-x}\text{Cu}_x(\text{PO}_4)_6\text{O}$ showing levitation at room temperature and atmospheric pressure and mechanism (2023), [arXiv:2307.12037 \[cond-mat.supr-con\]](https://arxiv.org/abs/2307.12037).
- [112] P. A. Lee and Z. Dai, Effective model for $\text{Pb}_9\text{Cu}(\text{PO}_4)_6\text{O}$ (2023), [arXiv:2308.04480 \[cond-mat.supr-con\]](https://arxiv.org/abs/2308.04480).
- [113] P. K. Jain, Superionic Phase Transition of Copper(I) Sulfide and Its Implication for Purported Superconductivity of LK-99, *The Journal of Physical Chemistry C* **127**, 18253 (2023).
- [114] S. Zhu, W. Wu, Z. Li, and J. Luo, First-order transition in LK-99 containing Cu_2S , *Matter* **6**, 4401 (2023).
- [115] A. B. Georgescu, Cu-doped $\text{Pb}_{10}(\text{PO}_4)_6\text{O}$, and V doped SrTiO_3 – a tutorial on electron-crystal lattice coupling in insulating materials with transition metal dopants (2023), [arXiv:2308.07295 \[cond-mat.str-el\]](https://arxiv.org/abs/2308.07295)